

Delay-induced homoclinic bifurcations in bistable dynamical systems

Natalia B. Janson* and Christopher J. Marsden

Department of Mathematics, Loughborough University, Loughborough LE11 3TU, UK

(Dated: April 9, 2022)

This paper is a prequel to our study of the possibility to solve global optimization problem by introducing a time delay into the classical gradient descent setting. Ultimately, we wish to explore the phenomena caused by delay in a dynamical system of the form $\dot{x}=f(x(t-\tau))$, $\tau>0$, where $f(z)$ is the negative of the gradient of some cost, or utility, function $V(z)$ with an arbitrary number of local minima of an arbitrary configuration. Using prior knowledge of the typical delay-induced effects in nonlinear dynamical systems, we hypothesize that the increase of delay should eliminate all local attractors and give rise to global chaos embracing all local minima, which could be exploited for optimization. In the subsequent paper studying multi-well $V(z)$ we demonstrate that this general idea has been correct. However, the details of bifurcations involved appear quite intricate and need to be first revealed for the simplest forms of utility functions having only two local minima, which is the goal of this paper. We discover that for a smooth f , the key phenomenon induced by the variation of the only control parameter τ is a homoclinic bifurcation coming in various versions. We reveal both the universal features of bifurcation scenarios realized for general smooth double-well landscapes V , and the distinctions between them determined by the local properties of V .

Keywords: delay differential equation, homoclinic bifurcation, global bifurcation

I. INTRODUCTION

The research presented here is a prerequisite to the full-scale exploration of a novel approach to optimization described in [1]. However, this paper represents a self-contained independent study of scalar bistable dynamical systems, whose right-hand sides are wholly delayed by a certain amount of time. These systems form a special class of dynamical models and manifest a plethora of interesting and important phenomena induced by delay. Their understanding will help to predict how the delay affects systems with many coexisting attractors, such as the ones arising in the context of optimization, which motivated this study.

Optimization is an important problem arising in many practical applications, which is mathematically reduced to formulating a cost, or utility, function generally dependent on several parameters. This function is usually assumed to have several local minima, and the task is to find the global minimum. Among the variety of approaches to solve this problem [2, 3], arguably the most popular ones are various extensions of the gradient descent [4], which is mathematically described by the following equation

$$\dot{\mathbf{x}} = -\nabla V(\mathbf{x}), \quad (1)$$

where $\mathbf{x}(t)\in\mathbb{R}^n$ is a state vector, $\dot{\mathbf{x}}=\frac{d\mathbf{x}}{dt}$, $V(\mathbf{x}): \mathbb{R}^n\rightarrow\mathbb{R}$ is a scalar energy, or landscape, function at least twice continuously differentiable [5], and ∇ is the gradient operator. In optimization problems, V is the cost function. If one launches (1) from randomly chosen initial conditions, the system spontaneously converges to the local,

but generally not to the global, minimum. To detect the global minimum, one of the the most efficient modifications of (1), called simulated annealing, involves trying a sequence of randomly chosen initial conditions and making probabilistic decisions on choosing the next step in the iterative process [6–9]. Thus, the procedure is inherently stochastic, and the solution of the respective equation converges to the global minimum “in probability”. Currently the most promising approach to optimization is quantum annealing, which could be implemented in quantum systems thanks to their ability to tunnel through potential barriers between the minima of some energy function. However, creation of such systems represents a colossal technological challenge, whereas in the existing quantum computers convergence to the global minimum (ground state) is also achieved with some probability and is not guaranteed [10]. Generally, none of the optimization techniques available are perfect, making the exploration of new approaches always valuable.

We propose an alternative modification of (1), which is both very simple and fully deterministic. Namely we delay the whole of the right-hand side of (1) by some amount τ . By combining bifurcation theory with the knowledge of typical delay-induced effects in dynamical systems, we hypothesize that an increase in delay should eliminate all local attractors in the new system and give rise to a single large attractor approaching all local minima of V , thus forcing the phase trajectory to eventually approach the global minimum regardless of the initial conditions. The latter would mimic the effect from adding large noise to (1) used in simulated annealing, but would be achieved in a fully deterministic manner. After that, by analogy with a slow decrease of noise intensity in simulated annealing, the delay could be slowly decreased to zero. We are examining whether, under this procedure, it is possible for the phase trajectory to automatically end up in the global minimum, and if so, under

*E-mail: N.B.Janson@lboro.ac.uk

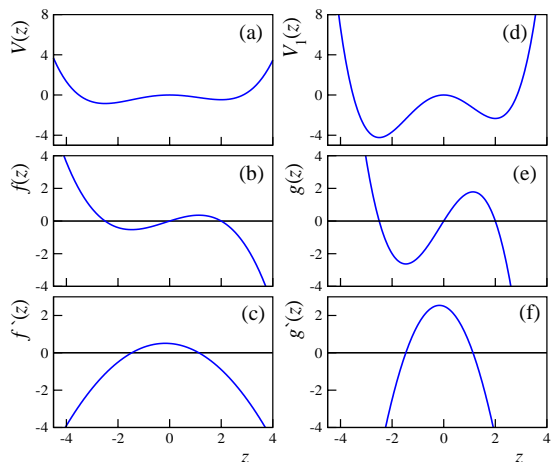


FIG. 1: Illustration of the relationship between equations (S1) with arbitrary τ , and (3) with $\tau=1$ and $g(z)=\tau f(z)$. For (S1) with $\tau=5$, left column shows (b) $f(z)=0.5z - 0.05z^2 - 0.1z^3$, (a) the respective landscape $V(z)$ and (c) $f'(z)$. Right column gives the respective functions for (3), namely, (e) $g(z)=5f(z)$, (d) the landscape $V_1(z)=5V(z)$ and (f) $g'(z)=5f'(z)$.

what conditions. For a cost function of a single argument with an arbitrary number and configuration of wells, this problem is addressed in [1]. However, before considering this difficult case, it is necessary to understand what happens if the landscape has the smallest meaningful number of wells, i.e. two wells. Here we consider the following equation

$$\dot{x} = f(x_\tau), \quad f(z) = -\frac{dV(z)}{dz}, \quad (2)$$

where $x, f, V, z \in \mathbb{R}$, $x_\tau = x(t - \tau)$, $\tau \geq 0$. In the current paper, V is a two-well smooth landscape function, and $V(z) \rightarrow \infty$ as $|z| \rightarrow \infty$.

Delay differential equations (DDEs) present a greater challenge for the analysis than ordinary differential equations (ODEs) because the dimension of their phase space is infinitely large and the time reversal is generally not permitted. It is generally impossible to accurately predict the behavior of non-linear DDEs analytically, and their studies heavily rely on numerical tools. The effects induced by delay greatly depend on the particular form of the DDE under study and on the exact way the delay is introduced. The latter makes it hardly possible to predict the dynamics even of a scalar equation with a single delay $\dot{x} = f(x, x_\tau)$ with $x, f \in \mathbb{R}$ and $x_\tau = x(t - \tau)$ for an arbitrary f . However, by extending the results from the qualitative theory of ODEs [11–13] it has been possible to qualitatively predict certain phenomena in special cases.

Namely, some predictions can be made for DDEs reducible to the form $\dot{x} = f(x_\tau) - g(x)$, often with $g(x) = \lambda x$ ($\lambda \in \mathbb{R}$) [14–19], or to an even simpler form (S1), for some special forms of f [20]. Most theorems formulated for (S1) assume that $\tau=1$ and f is amenable [20–29], i.e.

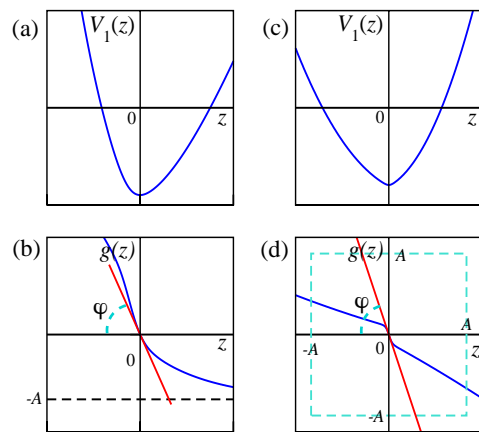


FIG. 2: Illustration of the theorems for the existence of periodic solutions in (3). In (b) and (d) blue lines show two suitable functions $g(z)$, and the upper panels (a) and (c) show the respective landscapes. Periodic solution exists if the slope of the tangent line to $g(z)$ at $z=0$ (red line) is $|g'(0)| = \tan(\varphi) > \frac{\pi}{2}$. (b) $g(z) = 8[e^{-(z+z^*)/10} - (1 + e^{-(z+z^*)})^{-1}]$ with $z^* \approx 1.69132$, and $g'(0) \approx -1.72664$. (d) $g(z) = [-(1 + e^{-10z})^{-1} + 0.5][\frac{z}{8} + 1]^2 - \frac{2z}{5}$, and $g'(0) = -2.9$.

the equation reads

$$\frac{dx}{dt} = g(x(t-1)), \quad g(z) = -\frac{dV_1(z)}{dz}. \quad (3)$$

However, introducing $t = s\tau$ and $x(t) = y(s)$ reduces (S1) to $\frac{dy}{ds} = \tau f(y(s-1))$, i.e. to (3) with $g(z) = \tau f(z)$ and the appropriate change in notations. Thus, the results valid for (3) can be easily adapted to (S1) by using the fact that the increase of τ in (S1) is equivalent to sharpening and deepening the wells of V_1 in (3), as illustrated in Fig. 1.

II. DELAY-INDUCED BEHAVIOR IN SIMPLE SYSTEMS

The idea of using delay for optimization is inspired by the knowledge of typical behaviors of (3) with relatively simple g . Although the key relevant theorems are available from literature, they have not been previously presented in a form accessible to the general reader, and not interpreted in the context of the landscape, which we need before explaining how we combine them in order to predict the behavior of (S1) with complex-shaped V . In sub-sections below three prominent special cases of g in (3) are considered, namely, monotonically decreasing with a single zero-crossing, and making two zero-crossings with a single maximum or a single minimum. We illustrate these cases with specially constructed examples.

A. Existence of a periodic orbit

In [21, 22], (3) was considered with $g(z)$ continuously differentiable and monotonically decreasing on some open neighbourhood of $z=0$, crossing zero at $z=0$, and in addition satisfying $zg(z)<0$ for all $z\neq 0$. I.e. $g(z)$ should be strictly positive for negative z and strictly negative for positive z . Therefore, the fixed point of (3) is at $x=0$.

In addition, $g(z)$ should either be bounded from below for all z (Fig. 2(b)), or satisfy $|g(z)|\leq A$ if $|z|\leq A$, where A is some positive constant (Fig. 2(d)). If $|g'(0)|>\frac{\pi}{2}$, then (3) has a non-zero periodic solution. In [24] the stability theorem for this periodic solution is proved. From the viewpoint of the landscape, to enable a periodic solution, the single well of the twice differentiable V_1 should be sufficiently sharp at the bottom (Fig. 2(a), (c)).

Note, that the quoted theorems require that $g(z)$ crosses zero at $z=0$. However, obviously, the same results can be adapted to $g(z)$ crossing zero at any z by making an appropriate change of variable. Thus, while the shape of g contains all the necessary information for the predictions, its localization on z -axis is not essential.

B. Existence of a homoclinic orbit of a fixed point

Equation (3) with a non-monotonic g was studied in [30, 31] but rewritten as

$$\frac{dx}{dt} = ah(x(t-1)), \quad a > 0, \quad h(z) = -\frac{dV_2(z)}{dz}. \quad (4)$$

Here, $h(z)$ is required to cross zero at $z=0$ from below to above, and at $z=-|b|$, $b\in\mathbb{R}$, from above to below. Parameter a controls the sharpness of the two extrema of V_2 . It has been shown that at certain a , in (4) there exists a stable periodic orbit around $x_2=-|b|$ (red circle in Fig. 3). As a increases, this orbit grows in size and, under some additional quantitative conditions on $h(z)$, at a equal to some critical value a^* can clash with the saddle fixed point at $x_1=0$ (green circle in Fig. 3) and form a homoclinic loop. At $a>a^*$ this orbit no longer exists.

This scenario is illustrated in Fig. 3 for a function $h(z)$, which has the required properties on the domain considered. With this h , (4) has two relevant fixed points $x_2=-2.5$ (red circle) and $x_1=0$ (green circle) corresponding to the local minimum and maximum of V_2 , respectively (Fig. 3(a)). At small a , the point x_2 is stable, but it loses stability at $a\approx 1.396$ at which $|ah'(-2.5)| = \frac{\pi}{2}$. The point x_1 is unstable for any $a>0$. At $a=2.24$ there exists a stable periodic orbit around x_2 shown in Fig. 3(f) in projection on the plane $(x(t), x(t-1))$, and the respective solution $x(t)$ is given in (e). At $a=a^*\approx 2.3765$ a homoclinic orbit is formed as the periodic orbit collides with x_1 , as shown in (d). In (c) the respective homoclinic solution $x(t)$ is shown, which departs from $x=0$ starting from some time instant in the past and approaches $x=0$ as $t\rightarrow\infty$ [44].

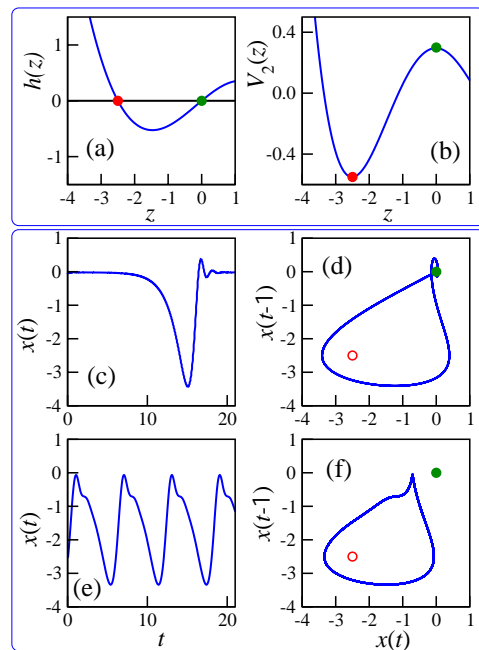


FIG. 3: Illustration of the theorem for the occurrence of a homoclinic bifurcation in (4), in which a stable periodic orbit collides with the saddle-focus fixed point to form a homoclinic loop. (a) Function $h(z)=0.5z-0.05z^2-0.1z^3$ in a suitable domain $z\in[-4, 1]$, which crosses zero at $z=0$ and at $z=-2.5$, (b) landscape V_2 . Filled circles indicate fixed points: red at the minimum, and green at the maximum of V_2 . (c) Homoclinic solution existing at $a=a^*\approx 2.3765$ and (d) the respective phase portrait. (e) Stable periodic solution and (f) the respective orbit at $a=2.24$.

One can interpret these events in the context of Shilnikov's theorem about the birth of a periodic orbit from the breakdown of the homoclinic loop of a saddle-focus fixed point [32, 33]. For $h(z)$ in Fig. 3(b) for a range of values of $a>0$, the fixed point $x_1=0$ of (4) is a saddle focus with a single real positive eigenvalue λ_1 , whereas all of its other eigenvalues are complex-conjugate with negative real parts (see Section III). According to Shilnikov's theorem for ODEs and a relevant study of a special form of (3) [29, 30], the breakdown of a homoclinic loop of a saddle-focus gives birth to a periodic orbit, if at the instant of homoclinic bifurcation the loop is "safe". The latter means that the saddle quantity of this saddle fixed point is negative, i.e. $\sigma=\lambda_1 + \text{Re}(\lambda_{2,3})<0$, where $\lambda_{2,3}$ are eigenvalues with the negative real parts closest to zero.

From this viewpoint, in (4) the homoclinic loop shown in Fig. 3(d) is formed as the parameter a decreases to its critical value a^* from above. As a is further decreased below a^* , from this homoclinic orbit a periodic orbit is born (Fig. 3(f)) provided the negativity of σ of the fixed point $x_1=0$. If $\sigma>0$, then in ODEs, according to Shilnikov, the breakdown of the homoclinic loop should produce chaos rather than periodic behavior.

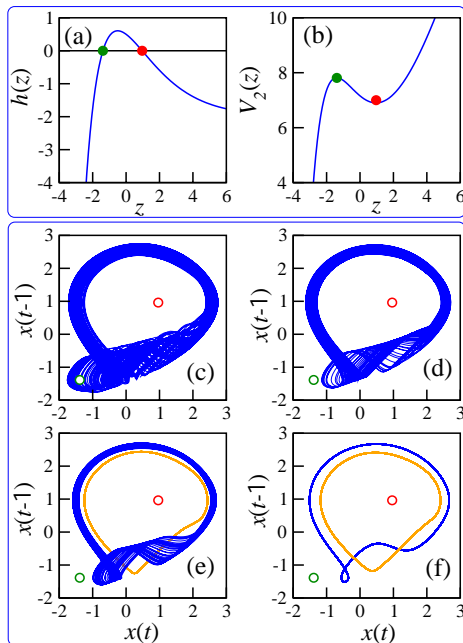


FIG. 4: Illustration of the theorem for the occurrence of a homoclinic bifurcation involving a saddle periodic orbit in (4), (5), to be referred to the bifurcation diagram in Fig. 5. (a) $h(z)$, and (b) the respective $V_2(z)$. (c)–(f) Phase portraits, with parameter a decreasing from (c) to (f), and circles showing fixed points x_1 (green) and x_2 (red). (c) Chaos from homoclinic bifurcation at the instant of birth at $a=3.913$, (d) chaos as the only attractor at $a=3.85$, (e) chaos coexisting with stable cycle (orange line) at $a=3.8325$, (f) two stable cycles of different origins coexisting at $a=3.773$.

C. Existence of homoclinic chaos from saddle cycle

Equation (3) with a relatively simple non-monotonic g can demonstrate a different sort of a homoclinic bifurcation arising from the closure of a stable and an unstable manifolds of a saddle periodic orbit, which can lead to chaos. In [28, 34] such chaos has been proved for very specific DDEs, for which a solution could be constructed analytically. Also, some general properties of function g of (4) have been outlined, which should lead to similar behavior. Namely, $g(z)$ should cross zero twice: from below to above at smaller z , and from above to below at larger z . Here we give an example of a suitable $h(z)$ in (4), which is equivalent to (3) with $g(z)=ah(z)$,

$$h(z) = \left(-\frac{1}{1 + e^{-\frac{z}{2}}} + e^{-\frac{z}{2}} \right) (2 - e^{-\frac{z}{2}}). \quad (5)$$

The function h is illustrated in Fig. 4(b), and the respective landscape V_2 is given in (a). Note, that there are two fixed points here, $x_1=-1.38629$ (maximum of V_2) and $x_2=0.962424$ (minimum of V_2). As explained in Section III, the saddle cycle can exist in this system only after x_1 undergoes Andronov-Hopf bifurcation whose condition is $(ah(z))' = \frac{3\pi}{2}$, which is satisfied at $a \approx 2.8274$.

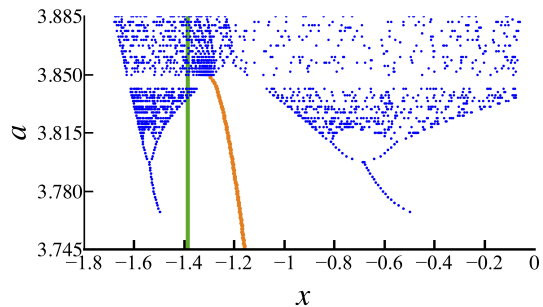


FIG. 5: A segment of bifurcation diagram of (4) with h given by (5), which for every value of a shows the local minima of the solution $x(t)$. Blue points show attractors originating from the homoclinic loop of the saddle cycle located around the saddle fixed point x_1 at the maximum of V_2 (green line). Orange points show attractor originating from the fixed point x_2 at the minimum of V_2 , which is outside the range of x of this figure. One can clearly see bistability for a inside $[3.77, 3.85]$, which means that two attractors of different origins coexist.

In (c)–(f) phase portraits are shown for (4) for various values of a . The homoclinic loop related to the saddle cycle around the saddle point (green circle) exists at a just above 3.913, but cannot be visualized. Attractors originating from this loop are shown by blue line, and attractors originating from the fixed point at the landscape minimum (red circle) are shown by green line. The description below can be associated with the bifurcation diagram in Fig. 5. At $a=3.913$ (c) and $a=3.85$ (d) chaos born from the homoclinic loop is the only attractor. At $a \in [3.77, 3.84]$ two attractors coexist. Panel (e) shows at $a=3.8325$ chaos born from the homoclinic loop of the saddle cycle together with the coexistent stable cycle born through Andronov-Hopf bifurcation from x_2 . In (f) at $a=3.773$ two coexisting stable cycles are given: the one born from homoclinic chaos in the inverse cascade of period-coupling bifurcations as a decreases (blue, compare with Fig. 5), and another born from x_2 as a increases (orange).

III. EIGENVALUES OF THE FIXED POINTS

From Sec. II it becomes apparent that in (S1) with a smooth V having minima and maxima, one should expect an interplay between periodic solutions born from the minima, and attractors born from homoclinic bifurcations associated with the maxima directly or indirectly. To predict the behavior of the solution near a minimum, or the one resulting from a homoclinic bifurcation related to a maximum, one needs to know the eigenvalues of the relevant fixed points. In Supplementary Note we performed the linear stability analysis of the fixed points of (S1) and showed that their eigenvalues λ_k can be expressed in terms of the Lambert function $W(z)$ with $z \in \mathbb{R}$

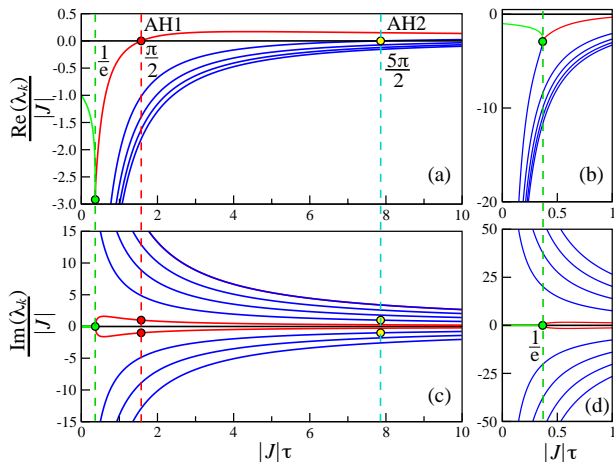


FIG. 6: (a)–(b) Real and (c)–(d) imaginary parts of the eigenvalues λ_k , normalized by $|J|$, of a fixed point corresponding to a minimum of the landscape $V(z)$ in (S1) as a function of $|J|\tau$. In (a)–(b) the leading eigenvalue λ_1 (green line) is real for $|J|\tau \in [0, \frac{1}{e}]$. At $|J|\tau > \frac{1}{e}$ all eigenvalues are complex. At $|J|\tau = \frac{\pi}{2}$ the real parts of a pair of leading eigenvalues (red line) cross zero signifying the first Andronov-Hopf (AH) bifurcation marked as AH1 in (a). At $|J|\tau = \frac{5\pi}{2}$ the second AH bifurcation takes place, marked as AH2 in (a). Left and right panels show the same functions in different ranges.

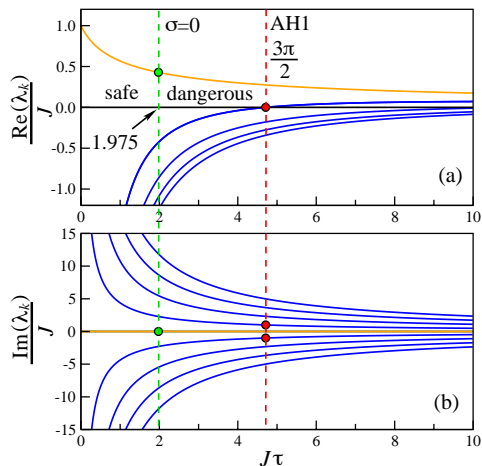


FIG. 7: (a) Real and (b) imaginary parts of the eigenvalues λ_k , normalized by J , of a fixed point corresponding to a maximum of $V(z)$ in (S1) as a function of $J\tau$. The leading eigenvalue λ_1 (orange line) is real for all τ . At $J\tau \approx 1.975$ the saddle quantity σ changes sign. At $J\tau = \frac{3\pi}{2}$ the first AH bifurcation takes place, marked as AH1.

and $W \in \mathbb{C}$ as

$$\lambda_k = \frac{W_k(J\tau)}{\tau} = \frac{JW_k(z)}{z}, \quad (6)$$

where $J = f'(x^*)$ and x^* is the fixed point. Function $W(z)$ has countably many branches, as illustrated in Fig. S2, and W_k is its k -th branch. Therefore, $\frac{\lambda_k}{J} = \frac{W_k(z)}{z} = \frac{W_k(J\tau)}{(J\tau)}$.

Figures 6 and 7 show eigenvalues of the fixed points at the landscape minimum and maximum, respectively (compare with Fig. S2).

Note, that at a landscape minimum $J < 0$, so with $\tau \geq 0$, $z = J\tau \leq 0$. However, in Fig. 6 for convenience we show $\frac{\lambda_k}{|J|} = \frac{W_k(-\tilde{z})}{\tilde{z}}$ as a function of $\tilde{z} = |J|\tau \geq 0$. For $|J|\tau \in (0, \frac{1}{e})$ the leading eigenvalue λ_1 (green line) is real and negative, whereas all other eigenvalues are complex with large negative real parts (this is well visible in (b) and (d)). Therefore, the fixed point is effectively a stable node, and the solution converges to it without oscillations. At $|J|\tau \in [\frac{1}{e}, \frac{\pi}{2})$ there is a pair of complex-conjugate leading eigenvalues with negative real parts (red line), so in the centre manifold of Andronov-Hopf (AH) bifurcation that occurs at $|J|\tau = \frac{\pi}{2}$, the fixed point is a stable focus and the solution converges to it in an oscillatory manner. The boundary between these two subtly different types of behavior is $\tau = \frac{1}{e}$, which is highlighted by vertical green dashed line in Fig. 6, and the respective values of real and imaginary parts of the eigenvalues are highlighted by green filled circles.

In Supplementary Note we derive the first condition for the first AH bifurcation of the fixed point x^* at the minimum of V (Eq. (S11))

$$\tau_{\text{AH1}} = \frac{\pi}{2|J|}, \quad (7)$$

and verify the second condition (Eq. (S18)). Equation (7) is consistent with the predictions for the existence of a periodic solution in (3) for a special form of $g(z)$ as discussed in Sec. II A. However, this result is more general and applies to a smooth f of any shape. Thus, Eq. (7) allows one to determine the value of τ at which it is possible for the stable cycle to be born from the fixed point at the landscape minimum. The first AH bifurcation, AH1, is highlighted by the vertical red dashed line in Fig. 6, and the respective values of real and imaginary parts of the eigenvalues are highlighted by red filled circles. At $\tau_{\text{AH2}} = \frac{5\pi}{2|J|}$ the second AH bifurcation occurs, as a result of which a saddle cycle could be born around the minimum. The second AH bifurcation, AH2, is highlighted with the vertical dashed cyan line in Fig. 6, and the respective values of real and imaginary parts of the eigenvalues are highlighted by yellow filled circles.

For a fixed point at the maximum of V , $J > 0$, and Fig. 7 shows $\frac{\lambda_k}{J} = \frac{W_k(J\tau)}{J\tau}$ as a function of $J\tau \geq 0$. One can see that, as also confirmed by the analysis in Supplementary Notes, at any $\tau \geq 0$ there is one real positive eigenvalue λ_1 (orange line), so this fixed point is always unstable for non-negative τ . However, it is important to appreciate that for $J\tau \in (0, \frac{3\pi}{2})$, this point is a saddle-focus with a one-dimensional unstable manifold and an infinite-dimensional stable manifold. As shown in (S19) of Supplementary Note, at $J\tau = \frac{3\pi}{2}$, or at

$$\tau_{\text{AH1}} = \frac{3\pi}{2J}, \quad (8)$$

the first AH bifurcation occurs, which is highlighted by a vertical red dashed line in Fig. 7, and the respective values of eigenvalues are marked by red filled circles. For visualization purposes, for $J\tau \in (0, \frac{3\pi}{2})$ we can mentally replace the stable infinite-dimensional manifold of the saddle-focus with a two-dimensional centre manifold of its first AH bifurcation. In this approximation, the given fixed point would represent a saddle-focus with a one-dimensional unstable manifold and a two-dimensional stable manifold, as schematically shown in Fig. 10(k). If there is a well of V nearby, the stable and unstable manifolds can form a homoclinic loop at some τ from inside $(0, \frac{3\pi}{2J})$. With this, Shilnikov's theorem for ODEs [32, 33] verified for a special form of (3) [29, 30], predicts that for a safe loop with $\sigma < 0$ (see IIB for the definition of σ and Shilnikov's theorem), which is true for $J\tau \in [0, 1.975)$, the homoclinic loop breaks down to form a stable periodic orbit. If the loop is dangerous with $\sigma > 0$, the resultant regime should be chaotic at least in ODEs [32, 33], although to the best of our knowledge this was not verified for DDEs.

Note, that at τ_{AH1} a saddle periodic orbit is born from the saddle point at the maximum, which is an intersection of a stable and an unstable manifolds. At larger τ the manifolds of this saddle orbit can form a loop, whose breakdown can give birth to chaos, as discussed in Sec. IIC.

IV. FROM SINGLE- TO DOUBLE-WELL LANDSCAPES

It follows from Sec. II that homoclinic bifurcations play a central role in DDEs (3) with non-monotonic $g(z)$ of even very simple shapes, and result in the disappearance of local attractors when g becomes sufficiently steep. The nature of the homoclinic bifurcations depend on the fine local features of g , but their occurrence seems inevitable as the steepness parameter grows. For (S1), an equivalent of the steepness parameter is τ , so the homoclinic bifurcations are expected to occur as τ grows.

We observe that a multi-well landscape function V in (S1) can be constructed by gluing together segments of landscapes considered in Sec. II and smoothing out all the joints. This observation leads us to suggest that the phenomena discussed in Sec. II should occur in different parts of the phase space of (S1) with a multi-well V . However, a multi-well function has a different quality as compared to a single-well one, so it is reasonable to also expect new phenomena not covered in Sec. II.

It is well appreciated that the apparatus based on the concept of the phase space, which has been originally developed for ODEs, in great many cases can be successfully applied to DDEs as well. Here we utilize the powers of the qualitative theory of ODEs [11–13] to predict and reveal the phenomena in (S1) with a double-well V . We illustrate our findings using two subtly distinct examples of V which manifest homoclinic bifurcations of different

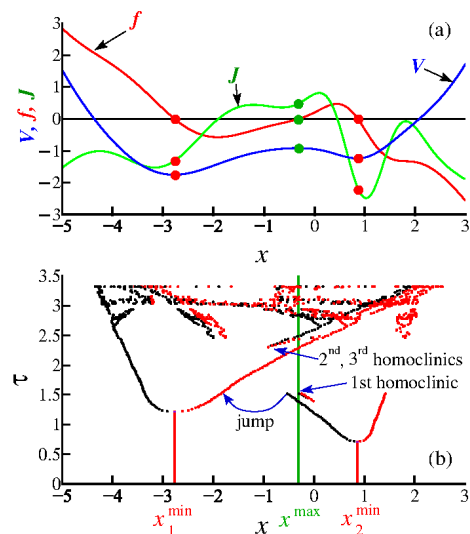


FIG. 8: (a) Functions $V(x)$ (blue line), $f(x)$ (red line) and $J(x)=f'(x)$ (green line) specified by (9). Red/green circles show positions of fixed points at the minima/maxima of V . (b) Bifurcation diagram of (S1), (9). Local minima/maxima of attractors are shown by black/red dots. Fixed points at the minima of V are shown by red vertical lines for τ at which they are stable, and the saddle-focus at the maximum of V is shown by green vertical line. As τ varies, in this system only safe homoclinic loops are formed by the manifolds of the saddle-focus fixed point x^{\max} .

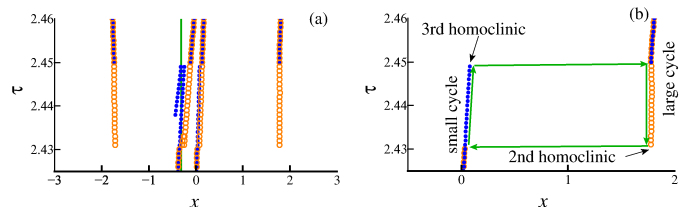


FIG. 9: (a) Segment of the bifurcation diagram in Fig. 8(b) illustrating 2nd and 3rd homoclinic bifurcations, bistability and hysteresis in (S1), (9). Circles show all maxima of the attractors (limit cycles): as τ increases (blue filled), and as τ decreases (orange empty). (b) The largest maxima of the attractors: as τ increases (blue filled), and as τ decreases (orange empty). Hysteresis loop is marked by green arrows.

kinds. However, our additional studies not reported here due to the lack of space, suggest the generality and reproducibility of the phenomena discovered for the landscapes with the same qualitative features. We construct the landscapes V of (S1) in such a way, that by adjusting parameters we could control their local features.

A. Homoclinic loop of a saddle fixed point

Here we consider bifurcations in (S1) with a double-well V and the respective $f=-V'$ specified as follows

$$\begin{aligned} V(x) &= -\frac{1}{2}e^{-2(x-1)^2} - e^{-0.5(x+3)^2} + 0.01(x+1)^4, \\ f(x) &= -2e^{-2(x-1)^2}(x-1) - e^{-0.5(x+3)^2}(x+3) \\ &\quad - 0.04(x+1)^3. \end{aligned} \quad (9)$$

The functions $V(x)$, $f(x)$ and $J(x)=f'(x)$ are shown in Fig. 8(a) by blue, red and green lines, respectively. Red circles indicate the positions of the fixed points at the landscape minima $x_1^{\min} \approx -2.77168$ and $x_2^{\min} \approx 0.864388$, which are stable at $\tau=0$, and green circle shows the fixed point at the landscape maximum $x^{\max} \approx -0.308654$, which is saddle at any $\tau \geq 0$.

The single control parameter here is τ , and the bifurcation diagram is shown in Fig. 8(b). Namely, red lines show the locations of x_1^{\min} and x_2^{\min} for the range of τ inside which they remain stable; at τ where the lines stop AH bifurcations occur in agreement with (7). Green line shows x^{\max} in the whole range of τ considered. For oscillatory attractors, red/black dots indicate local maxima/minima of $x(t)$, which constitute the projections of the Poincaré sections defined as $\dot{x}=0$, $\ddot{x}<0/\ddot{x}>0$, respectively. Note, that this diagram is different from the classical bifurcation diagrams, such as the one in Fig. 5, which usually show only one kind of the attractor extrema. We show both kinds of the extrema because we need to illustrate how the sizes of the limit cycles borm from AH bifurcations grow with τ , and how the attractors approach the saddle point x^{\max} , which allows us to detect homoclinic bifurcations. Altogether there are three homoclinic bifurcations, as indicated in Fig. 8(b). Figure 9 shows a segment of the bifurcation diagram around the 2nd and 3rd homoclinic bifurcations.

In (S1) with V and f given by (9), within the range of τ shown in Fig. 8(b), the point x^{\max} is of a saddle-focus type with $J(x^{\max}) \approx 0.490368$. Namely, it has a single real positive eigenvalue λ_1 corresponding to a one-dimensional unstable manifold, and countably many complex-conjugate eigenvalues with negative real parts corresponding to a stable manifold of co-dimension one. The homoclinic bifurcations in this system occur as the manifolds of x^{\max} close to form homoclinic loops at certain values of τ . From these loops limit cycles are born as τ decreases or increases.

The key components of homoclinic bifurcations are manifolds, and it is their reconfiguration which induces drastic changes in the observed system behavior. Importantly, different basins of attraction are separated by the *stable* manifolds. In this subsection, the separatrix would be the stable manifold of x^{\max} . Therefore, to understand if and how local attractors in (S1), (9) can disappear as τ grows, one needs to understand how both unstable and stable manifolds are reconfigured. Whereas the attractors of nonlinear DDEs can be detected numeri-

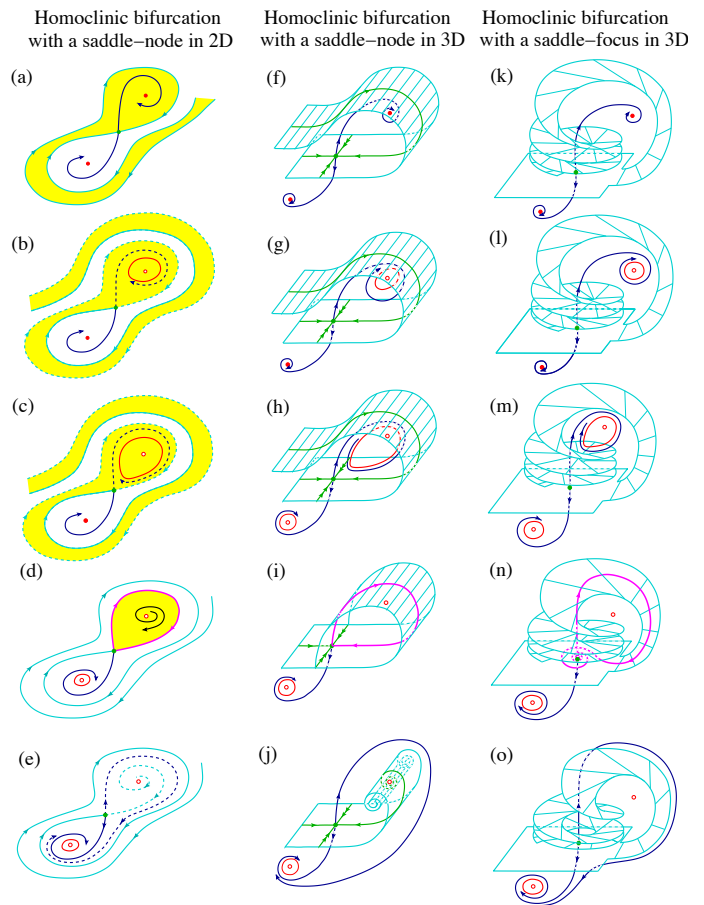


FIG. 10: Schematic illustration of the 1st homoclinic bifurcation in (S1), (9). **Right column:** sketch of attractors, fixed points and manifolds of (S1), (9) around the *saddle-focus* fixed point x^{\max} (green circle). The value of τ increases from (k) to (o), and the homoclinic loop (magenta line) is shown in (n). Other objects are: stable (cyan surface) and unstable (blue line) manifolds of the saddle-focus, stable fixed points (filled red circles), same fixed points above AH bifurcation (empty red circles), and stable cycles (red line). **Left and middle columns:** same objects as in the right column in some fictional systems of dimension two (left) or three (middle), with the saddle-focus replaced by a saddle-node. **Left column only:** yellow and white shades show basins of attraction of two different attractors; dashed lines in (b), (c), (e) show manifolds involved in homoclinic bifurcation. **Middle column only:** green line with double arrows is *strong* stable manifold of x^{\max} contained in the stable 2D manifold, and green lines with single arrows are trajectories on the stable 2D manifold, which approach x^{\max} along its eigenvector corresponding to the larger of two negative eigenvalues. More explanations are in text.

cally with relative ease, revealing and plotting manifolds of such systems is a challenge. A method to reveal 2-dimensional manifolds in nonlinear ODEs have been introduced in [35], and a technique to obtain *unstable* manifolds in DDEs was described in [36]. However, the phase space of a DDE is infinite-dimensional, implying that the

stable manifold of x^{\max} has dimension infinity and is thus highly challenging to detect and to depict. Moreover, revealing a stable manifold would require reversing time, which is generally not possible in DDEs [37]. With this, to the best of our knowledge, there are no techniques available to date to numerically obtain stable manifolds of DDEs.

In order to schematically illustrate homoclinic bifurcations in our DDEs, we can proceed by analogy with a centre manifold reduction in ODEs [38]. Namely, we can assume that the dynamics on the infinite-dimensional stable manifold of the saddle-focus fixed point x^{\max} of (S1), (9) can be approximated by the dynamics on the two-dimensional manifold associated with the leading pair of complex-conjugate eigenvalues of this point. We thus visualize the given saddle-focus (green filled circle in Fig. 10(k)) as an intersection of the latter two-dimensional stable manifold (cyan surface, a segment is shown) and the one-dimensional unstable manifold (blue line) associated with the only real and positive eigenvalue of this point. The stable manifold is the boundary between the attractor basins of two attractors (red filled circles or red lines). The way the stable manifolds rearrange themselves during homoclinic bifurcations of a saddle-node and a saddle-focus in a 3-dimensional system has been revealed numerically in [39] and [40], respectively. Here we apply these findings in order to understand and predict reorganization of manifolds in (S1), (9).

Below we explain the results of numerical simulations of (S1), (9) shown in Fig. 11 with sketches of manifolds and attractors. Start with the 1st homoclinic bifurcation. As τ grows from zero, the following events occur. At $\tau \in [0, 0.7155]$ there are two coexisting stable fixed points (Fig. 10(k)) at x_1^{\min}/x_2^{\min} below/above the stable manifold of x^{\max} . At $\tau \approx 0.7155$, x_2^{\min} undergoes AH bifurcation and the stable cycle is born from it. The situation just above this bifurcation is illustrated in Fig. 10(l), where red line above the stable manifold shows the newly born cycle. At $\tau \approx 1.208$, x_1^{\min} undergoes AH bifurcation and the stable cycle is born from it, which for a slightly larger τ is given by red line below the cyan surface in Fig. 10(m) (compare with Fig. 11(a)). With this, the first limit cycle (upper red line in 10(m) and turquoise in 11(a)) has grown in size and stretched towards the saddle focus. At $\tau \approx 1.53$, the homoclinic bifurcation occurs, namely, the limit cycle around x_2^{\min} collides with x^{\max} , the unstable manifold of the latter “sticks” to its own stable manifold and forms a homoclinic loop (magenta lines in 10(n) and in 11(b)–(c)). This bifurcation is identical to the one illustrated in Figs. 3(d), (f).

At $\tau > 1.53$, the unstable manifold appears to the other side of the stable one (Fig. 11(o)). The limit cycle around x_2^{\min} has been destroyed by the homoclinic bifurcation, and the only attractor left is the limit cycle around x_1^{\min} , to which both unstable manifolds of x^{\max} converge (10(o) and 11(d)).

One could mentally revert the sequence of events and

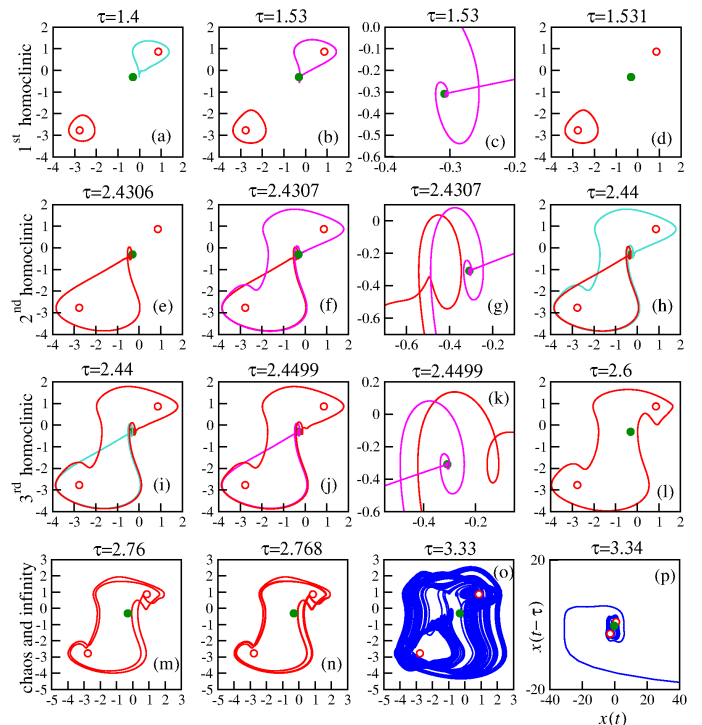


FIG. 11: Phase portraits of (S1), (9) illustrating bifurcation diagrams in Figs. 8 and 9 with τ given in panels. Notations are: fixed points $x_{1,2}^{\min}$ (red circles) and x^{\max} (green circle); filled/empty circles indicate points below/above AH bifurcations; attractors (read and turquoise lines), and homoclinic loops (magenta line). **1st row:** (a) Before, (b)–(c) at, and (d) after 1st homoclinic bifurcation. Small cycle around x_2^{\min} (turquoise line in (a)) collides with x^{\max} to form a homoclinic loop (magenta line in (b)–(c)) around x_2^{\min} , and disappears (d). **2nd row:** (e) Before, (f)–(g) at, and (h) after the 2nd homoclinic bifurcation. (e) Small cycle around x_1^{\min} is the only attractor, (f)–(g) homoclinic loop of x^{\max} , (h) large cycle born from homoclinic loop (turquoise line) coexisting with small cycle around x_1^{\min} (red line). **3rd row:** (i) Before, (j)–(k) at, and (l) after 3rd homoclinic bifurcation. (i) Large and small cycles coexist, (j)–(k) cycle around x_1^{\min} collides with x^{\max} and forms a homoclinic loop, (l) large cycle is the only attractor. **4th row:** (m) 2-cycle, (n) 4-cycle, (o) Chaos embracing all fixed points at large τ , and (p) trajectory goes to infinity at even larger τ .

consider τ decreasing from above to below 1.53. In that case, at $\tau > 1.53$ there would be no attractor in the close vicinity of x^{\max} , at $\tau \approx 1.53$ the manifolds of x^{\max} form a homoclinic loop, and at $\tau < 1.53$ an attractor is born from this loop as a result of its breakdown. Note that the quantity $J(x^{\max})\tau \approx 0.75 < 1.975$, hence the saddle-focus homoclinic loop is “safe” here as described in Sec. III (see Fig. 7(a)). Therefore, according to Shilnikov’s theorem [32, 33], the attractor born from the loop must be the limit cycle, which is indeed the case.

Note that close to the homoclinic bifurcation, part of the stable manifold of x^{\max} returns to the vicinity of

x^{\max} from above and takes the shape of an open helicoid with a finite number of turns (see upper part of Fig. 10(k)-(m)), with turns coming closer to each other as they come closer to the saddle-focus, as numerically demonstrated for a 3-dimensional dynamical system in [40]. At the instant of homoclinic bifurcation (n), the helicoid becomes closed and develops an *infinite* number of turns, such that the distance between the consecutive turns becomes smaller as the turns come closer to x^{\max} . At the same instant, the unstable manifold “sticks” to this closed helicoid and forms a loop (n). After the homoclinic bifurcation, the helicoid opens and possesses a finite number of turns again (o). As a result of homoclinic bifurcation, the one-dimensional unstable manifold (blue line) “permeates” through the stable one (cyan surface), and the latter no longer separates basins of attraction.

Figures 10(k)-(o) schematically show only a small portion of the stable manifold near the homoclinic loop. However, in reality this manifold has an even more complex shape. E.g. in (o) a part of this manifold should unwind from the vicinity of the unstable fixed point (empty circle in the upper part), but we cannot show this without overloading the figure. Also, this manifold extends well beyond the boundaries shown and has a similarly complex structure in the lower parts of Figs. 10(k)-(o), which we again do not show for the sake of clarity. Thus, the complexity of the shape of the stable manifold of the saddle-focus prevents us from illustrating this bifurcation in full. However, reorganization of the manifolds *away* from the homoclinic loop during this bifurcation would be qualitatively the same if the saddle-focus is replaced by a saddle node, whose manifolds have a simpler shape and are easier to depict. In order explain how the manifolds are being reorganized globally, in left and middle columns of Fig. 10 we show the same sequence of events occurring in some fictional 2-dimensional and 3-dimensional systems, respectively, with a saddle-node and the simplest orientable homoclinic bifurcation. The middle column illustrates a 3-dimensional system with a 2-dimensional stable manifold (cf. with right column) and in (f)–(h) shows how the stable manifold separates two attractor basins. Panel (j) shows the stable manifold unwinding from the unstable point in the upper part, and the stable manifold in (o) should do the same.

However, in a 3-dimensional visualization we still cannot extend the stable manifold too much without obscuring the view of the saddle vicinity, and cannot mark different basins of attraction. The left column of Fig. 10 illustrates the same events as the middle column, only in a 2-dimensional system with two one-dimensional manifolds of the saddle-node. Here we can extend the stable manifold well beyond the close vicinity of the saddle fixed point, and highlight different basins with different shades. Namely, the basin of attractor vanishing through the bifurcation is shaded yellow, and the other basin is white. In (b)–(c) and (e) dashed lines mark the manifolds involved in the homoclinic bifurcation. After the homoclinic loop is formed (d), there is no attractor in the

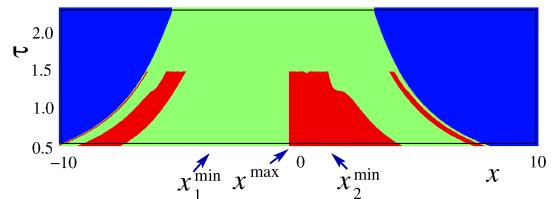


FIG. 12: Basins of attraction of (S1), (9) with safe homoclinic loops, as a function of τ . Different shades mark points x such that, from initial conditions $\varphi(t)=x$, $t \in [-\tau, 0]$, the phase trajectory converges to the following attractors: infinity (blue), fixed point or limit cycle around x_1^{\min} (green), fixed point or limit cycle around x_2^{\min} (red). Above $\tau=1.53$ there is no local attractor around x_2^{\min} . Note the stripy structure of the basins below $\tau=1.53$.

upper part of the picture (e).

Note, that Fig. 10 (left column) shows that the stable manifold makes more than one turn around the three fixed points, which was hypothesized for the given system based on experience with ODEs, and implies that both basins of attraction should have a stripy structure. With this, numerical simulation of (S1), (9), as well as of several similar DDEs, revealed that at positive τ from some initial conditions such systems systematically go to infinity. Although there are no tools to obtain a stable manifold of a DDE directly, one can bear in mind that such a manifold would be the boundary between different attractor basins. Then finding the basins could be another way to reveal the shape of the stable manifold, as was done in [41] for a 4-dimensional system. The basin of attraction in (S1) is a set of all initial functions $\varphi(t)$, $t \in [-\tau, 0]$, such that all solutions starting from these functions converge to the given attractor. It is a subset of an infinite-dimensional phase space and difficult to visualize. However, we utilize an approach of [42, 43] and consider only a subset of all possible initial conditions, namely, functions of a certain class parametrized by a finite number of parameters. In our case we choose the simplest class of constant initial functions, $\varphi(t)=x=\text{const}$, $t \in [-\tau, 0]$. Such functions can be directly compared with the positions of fixed points.

The basins of attraction of (S1), (9) are given in Fig. 12 for a range of τ in the vicinity of the first homoclinic bifurcation. The striking feature of this plot is the large basin of attraction of infinity (blue shade), which expands with growing τ . Below $\tau=1.53$, in addition to infinity, there are two attractors on different sides of x^{\max} , and on the plot we do not distinguish between fixed points and limit cycles. At $\tau \approx 1.53$ the red basin of attraction collapses due to the first homoclinic bifurcation, and at $1.53 < \tau < 2.43$ besides the infinity there is only one attractor around x_1^{\min} . Note, that Fig. 12 confirms the suggestion that the basins of attraction are stripy, and therefore the stable manifold of x^{\max} makes several turns around the three fixed points. In what follows, we will bear in mind that the infinity is present as some kind of an at-

tractor at all values of $\tau > 0$. However, when discussing attractors, we will mention only those at finite locations around the fixed points.

Next, consider the second and the third homoclinic bifurcations, which in Fig. 8(b) one can hardly distinguish because since they occur at very close values of τ . However, their roles are very different, since the second bifurcation creates a large attractor embracing all fixed points (Fig. 11(e)–(h)), whereas the third bifurcation destroys the last local attractor, which is the limit cycle around x_1^{\min} (Fig. 11(i)–(l)). Within a range $\tau \in [2.4307, 2.4499]$ the local and the global attractors coexist, and the system displays hysteresis, as demonstrated in Fig. 9.

Namely, at $\tau \in (1.53, 2.4307)$ the only attractor is the limit cycle localised around x_1^{\min} (Fig. 11(d)–(h), red line). At $\tau \approx 2.4307$ the second homoclinic bifurcation occurs, from which a large limit cycle is born ((f)–(g) magenta line, (h) turquoise line). When τ increases to 2.4499, the third homoclinic bifurcation takes place, which eliminates the small limit cycle on the left (Fig. 11(j)–(k), magenta line). At $\tau \in (2.4499, 3, 33]$, the system has a single large attractor enclosing all fixed points. This attractor is initially a limit cycle of period one (Fig. 11(l)), but with increasing τ it undergoes a cascade of period-coupling bifurcations (Fig. 11(m)–(n)) and becomes chaotic (o). Note, that the phase trajectory on the chaotic attractor visits the close vicinities of all three fixed points. As τ exceeds 3.33, the chaotic attractor disappears and the trajectory goes to infinity (p). We cannot specify the exact reason for this, and can only hypothesize that the manifold bounding the basin of attraction of chaos appears involved in some global bifurcation. Since we cannot visualize this manifold, we cannot verify our hypothesis. However, our studies of a considerable number of systems of the form (S1) with various multi-well landscapes V suggest the universality of this phenomenon. Namely, it seems that in such systems, as τ becomes sufficiently large, a chaotic attractor enclosing all extrema of V is born (although it might turn into a periodic one at even larger τ in agreement with the laws of chaotic dynamics); when τ is increased further, the large attractor is inevitably destroyed and the trajectory escapes to infinity from all initial conditions.

Figure 9 illustrates multistability and hysteresis reported above. Namely, Fig. 9(a) shows all local maxima of an attractor as a function of τ as τ increases (blue filled circles) and as τ decreases (orange empty circles). We start from the small limit cycle at $\tau = 2.425$ (blue circles) and stay on it until $\tau \approx 2.4499$, at which it disappears in the third homoclinic bifurcation and the trajectory jumps to the large cycle (filled and orange circles superimposed above $\tau = 2.4499$). As one starts from the large cycle at $\tau = 2.46$ and decreases τ gradually to $\tau = 2.4307$, the large cycle vanishes via a homoclinic bifurcation and the trajectory jumps to the small cycle. Bistability and hysteresis are clearer visible in (b) where only the largest maxima of the attractors are given.

The formation of the large limit cycle involves a differ-

ent pair of manifolds of the saddle-focus x^{\max} . Inspired by the visualisations of the finite-dimensional stable and unstable manifolds of the saddle-focus in a 3-dimensional system of ODEs in [40] in the vicinity of a small homoclinic loop, in Fig. 13 we sketch the respective manifolds in centre manifold reduction in the vicinity of a *large* homoclinic loop of (S1), (9). Panels (a)–(b) illustrate the situation just before the second (large) homoclinic loop is formed, and (c)–(d) illustrates the instant of the large loop formation. The picture of the manifolds here is even more complex than near the small homoclinic loop shown in Fig. 10 (right column) because of the spiralling of the stable manifold as it approaches the saddle focus from both sides. However, away from the saddle focus, the stable manifold is qualitatively similar to the one of a saddle-node, which we illustrate near a large orientable homoclinic loop in Fig. 14 (a)–(b), (f)–(g) for comparison.

The stable manifold (cyan surface) wraps itself around all the three fixed points making more than one layer. As a result, before the large homoclinic loop, the unstable manifold of the saddle-focus goes between the two layers of the stable manifold towards the local attractor near x_1^{\min} (see Figs. 13(a)–(b) and 14(a), (f)). At the instant of homoclinic bifurcation at $\tau \approx 2.4307$, a segment of the stable manifold collides with the saddle-focus and captures the unstable manifold, which now forms a large safe homoclinic loop (compare Figs. 11(f)–(g), 13(d) and 14(b), (g)). Note, that at the instant of bifurcation, the helicoid segment of the stable manifold containing the homoclinic loop makes an infinite number of turns as it approaches the saddle focus (Fig. 13(d)). As τ grows, the loop disappears and gives birth to a large limit cycle embracing all three fixed points (compare turquoise line in Fig. 11(h) with the large cycle in red in Figs. 14(c), (h)).

The third homoclinic bifurcation is qualitatively the same as the first one. Namely, at $\tau \approx 2.4499$ the small limit cycle around x_1^{\min} collides with the saddle focus and forms a safe homoclinic loop (compare Figs. 11 (b) and (j), and Fig. 10(i), (n) with Figs. 14 (d), (i)). At $\tau > 2.4499$ there are no more local attractors in the system.

We also studied the phenomena induced by the increase of τ in a slightly different system of the form (S1) with a double-well landscape $V(x)$, in which at the instants of homoclinic bifurcations the saddle focus was below AH bifurcation, but had a positive saddle quantity. According to Shilnikov's theorem for ODEs [32, 33], in such cases the homoclinic loops are expected to be dangerous, and their breakdown should lead to the formation of chaotic attractors. However, to the best of our knowledge, this result has not been verified for DDEs. Our numerical studies did not reveal any obvious differences between the sequence of bifurcations in the systems of the form (S1) with double-well landscapes V with dangerous or safe homoclinic loops, and the observed phenomena looked very similar when studied with the same numer-

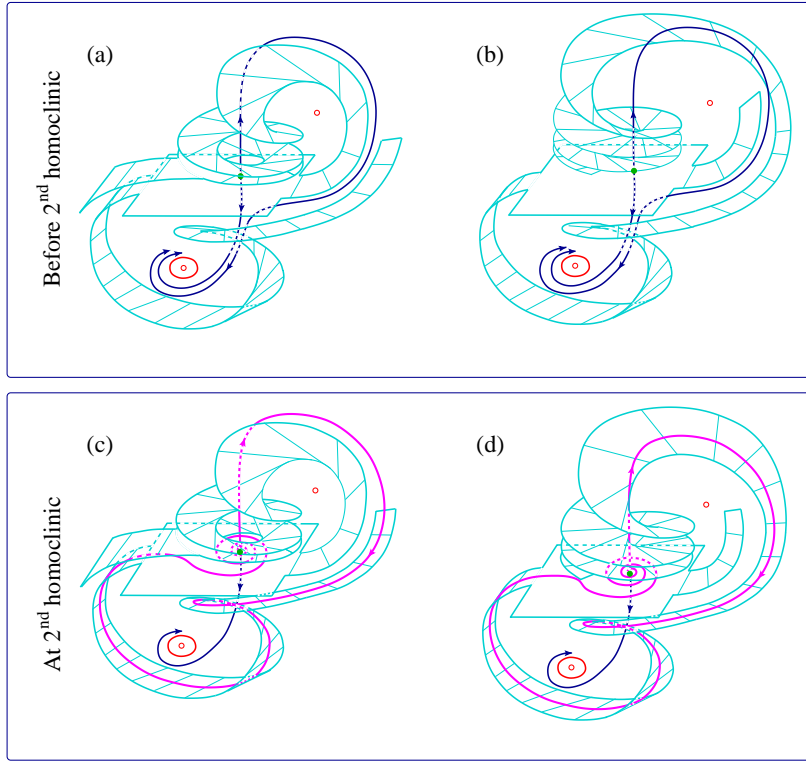


FIG. 13: Schematic illustration of the 2nd homoclinic bifurcation in (S1), (9), i.e. of formation of a large safe homoclinic loop (magenta line) of the saddle-focus x^{\max} (green filled circle). Stable (cyan surface) and unstable (blue line) manifolds of x^{\max} are shown just before (a)–(b) and at (c)–(d) homoclinic bifurcation; unstable fixed points at $x_{1,2}^{\min}$ (empty red circle). Each pair of panels (a)–(b) and (c)–(d) corresponds to the same values of τ . Upper parts of each panel show segments of the stable manifold, which are not involved (a), (c), and involved (b), (d), in the homoclinic bifurcation. The helicoid-shaped segments of the stable manifold approaching the saddle-focus from above make a finite (a)–(c), or an infinite (d), number of turns.

ical accuracy. Thus, whether the dangerous homoclinic loop gave birth to chaos or not, it did not affect the order of bifurcations, and the same key phenomena were observed. With this, a separate study would be needed to reveal whether dangerous loops indeed give birth to chaos in DDEs of the form (S1).

B. Homoclinic loop of a saddle cycle

Here, we consider Eq. (S1) with a subtly different version of a double-well landscape V and the respective $f = -V'$ specified as follows

$$\begin{aligned} V(z) &= -\frac{1}{2}e^{-2(x-1)^2} - e^{-0.5(x+3)^2} + 0.01(x+1)^4 \\ &\quad + 0.2e^{-10x^2}, \\ f(z) &= -2e^{-2(x-1)^2}(x-1) - e^{-0.5(x+3)^2}(x+3) \\ &\quad - 0.04(x+1)^3 + 4e^{-10x^2}x. \end{aligned} \quad (10)$$

The functions $V(x)$, $f(x)$ and $J(x) = f'(x)$ are shown in Fig. 15(a) by blue, red and green lines, respectively. The essential difference of the V above from the one of (9)

is that at the saddle-focus fixed point $x^{\max} \approx -0.0420246$ the Jacobian J takes a much larger value, which results in the AH bifurcation occurring at much smaller value of τ , namely at $\tau \approx 1.037783$. Similarly to (S1), (9), in Eqs. (S1), (10) the increase of τ leads to a sequence of three homoclinic bifurcations (compare Figs. 8(b) and 15(b) which have the same notations). However, in the latter system these involve the manifolds of the saddle cycle around x^{\max} , rather than of x^{\max} itself, as explained in II C.

The first homoclinic bifurcation is illustrated in more detail in Fig. 16 and can be compared with Fig. 5. The first small homoclinic loop of the saddle cycle is formed at $\tau \approx 1.118$, and as τ is *decreased*, it breaks down to form a chaotic attractor (blue dots in Fig. 16 and blue line in Figs. 17(b)–(c)), which with the further reduction of τ undergoes an inverse sequence of period-doubling bifurcations transforming it into a limit cycle (blue line in Fig. 17(a)). The latter cycle disappears at $\tau \approx 1.02$. As τ grows, the sequence of events is initially similar to the one in Fig. 8(b), i.e. at $\tau \approx 0.705$ a stable cycle is born through AH bifurcation from x_2^{\min} , which grows in size with τ (orange dots in Fig. 16 and orange line in Fig. 17(a)). However, at $\tau \approx 1.038$ this cycle disappears, possibly in the

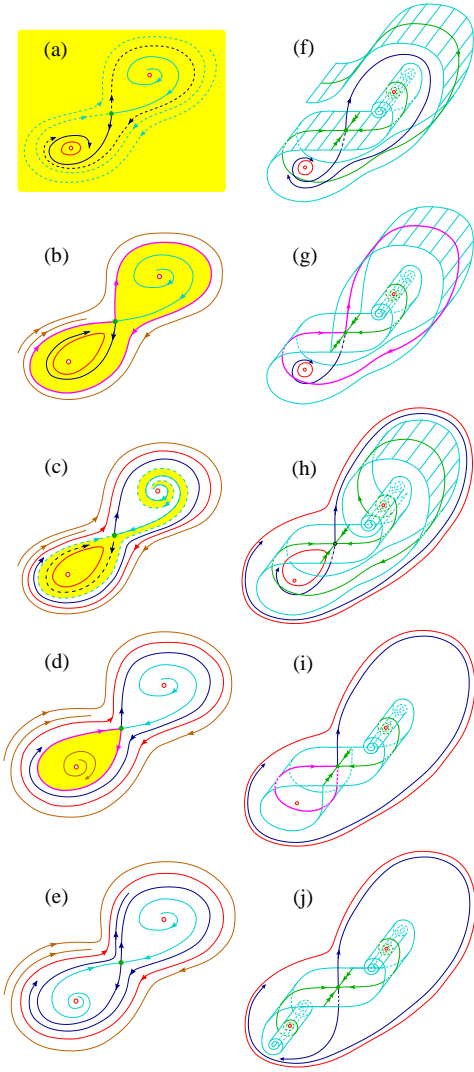


FIG. 14: Schematic illustration of homoclinic bifurcations in some fictional 2- (left column) and 3-dimensional (right column) systems with a saddle-node, which are similar to the 2nd and 3rd homoclinic bifurcations of the saddle-focus in (S1), (9) with safe loops forming as τ is increased from 2.425 to 2.46. Notations are as in Fig. 10, and in addition in (b)–(e) brown line shows a typical phase trajectory. Here, *away* from the saddle-node, the stable manifold (cyan line or surface) behaves in a qualitatively the same manner as with a saddle-focus, compare (f)–(g) with Fig. 13.

collision with the saddle cycle around x^{\max} . In a narrow range $\tau \in [1.02, 1.038]$ two attractors coexist around x_2^{\min} , but this multistability does not affect considerably the general picture of bifurcations predicted for a system with a double-well landscape.

Namely, as τ increases beyond the value of the first homoclinics 1.118, all of the local attractors on one (here right) side of x^{\max} cease to exist, and the system has a single local attractor around x_1^{\min} (red filled circle in Figs. 17(d)–(e)). At some higher value of $\tau \approx 2.49650$,

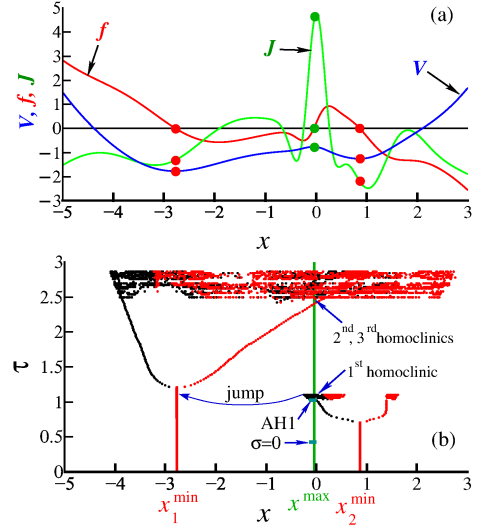


FIG. 15: (a) Functions $V(x)$ (blue line), $f(x)$ (red line) and $J(x)=f'(x)$ (green line) specified by (10). Red/green circles show positions of fixed points at the minima/maxima of V . (b) Bifurcation diagram of (S1), (10). Notations are as in Fig. 8(b). As τ varies, homoclinic loops are formed by the manifolds of the saddle cycle around x^{\max} born at the point AH1.

the second (large) homoclinic loop is formed by another pair of manifolds of the saddle cycle around x^{\max} , which gives birth to a large chaotic attractor embracing all three fixed points (blue line in Figs. 17(f)–(h)). In a narrow range $\tau \in [2.49650, 2.4968337]$ two attractors coexist: the only remaining local attractor around x_1^{\min} and the large attractor, see blue and cyan lines in Fig. 17(i), respectively. At $\tau \approx 2.4968337$ a small homoclinic loop is formed by the manifolds of the saddle cycle thanks to the left-hand local attractor approaching this cycle (blue line in Figs. 17(j)–(k)). At higher τ the last of the local attractors disappears, and the only remaining attractor is the large chaos (cyan line in Fig. 17(l)), which survives until $\tau \approx 2.87$ (blue line in Figs. 17(m)–(n)). Like in (S1), (9), as τ reaches a certain threshold (here 2.876), even this large attractor vanishes and the phase trajectory goes to infinity (blue line in Fig. 17(o)).

V. DISCUSSION AND CONCLUSION

As a prequel to our study of the possibility to exploit the time delay for global optimization by modifying the “gradient descent” setting with a multi-well cost function V [1], here we considered in detail its simplest case. Namely, we explored the delay-extended gradient descent for a cost function depending on only a single parameter and having only two minima. Although this case does not seem too difficult for optimization, the respective delay differential equation (DDE) demonstrates a plethora

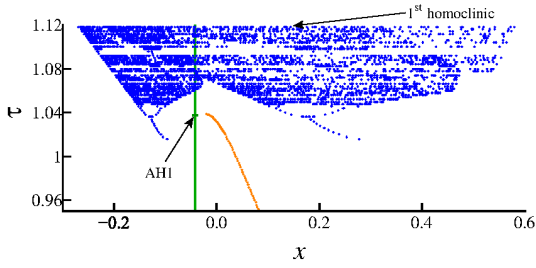


FIG. 16: A segment of the bifurcation diagram in Fig. 15(b) illustrating bistability, hysteresis, and the 1st homoclinic bifurcation in (S1), (10) inside the right well of V (cf. with Fig. 5). Green line shows x^{\max} , and dots show the local minima of the attractors: limit cycle (orange) born via the first AH bifurcation from x_2^{\min} (outside the range of this figure), and attractor developed from the homoclinic loop of the saddle cycle via 1st homoclinic bifurcation as τ decreases from 1.118 (blue). AH1 is the first AH bifurcation of x^{\max} , which gives rise to the saddle cycle with its manifolds forming a loop at $\tau \approx 1.118$.

of complex phenomena which needed to be revealed before our approach could be applied to more general cost functions. For a general nonlinear DDE with an arbitrary nonlinearity and an arbitrary dependence on delay, it is usually impossible to predict the behavior as the delay changes. However, we hypothesized and verified that for a special class of nonlinear models (S1), in which the *whole* of the right-hand side of a gradient dynamical system is delayed by the same amount, it is possible to make qualitative predictions of the phenomena induced by the increase of the delay. Thus, besides being relevant to the optimization problem, our research makes a useful contribution into the theory of bifurcations in delay differential equations.

Specifically, we tested and confirmed our initial hypothesis, that the increase of the delay τ should lead to a chain of homoclinic bifurcations leading to the disappearance of attractors localised around the minima of V , and to the eventual birth of a large attractor embracing all local minima, which forces the system to visit the vicinity of every minimum, including the global minimum, as time goes by. The latter resembles the effect from a random term within simulated annealing, but is achieved in a purely deterministic manner. It also has some similarity with quantum annealing performed thanks to the ability of particles to tunnel the potential barriers between the local minima of energy function. In our case, thanks to the delay, the barrier between the two minima of the cost function effectively disappears enabling the system to freely wander between both of the minima.

We discovered that depending on the relative sharpnesses of the landscape minima and the maximum, the homoclinic bifurcations vary in their details. Namely, the local attractor around one of the minima may collide either with the maximum itself, or with the saddle cycle born from this maximum. Prior to the disappear-

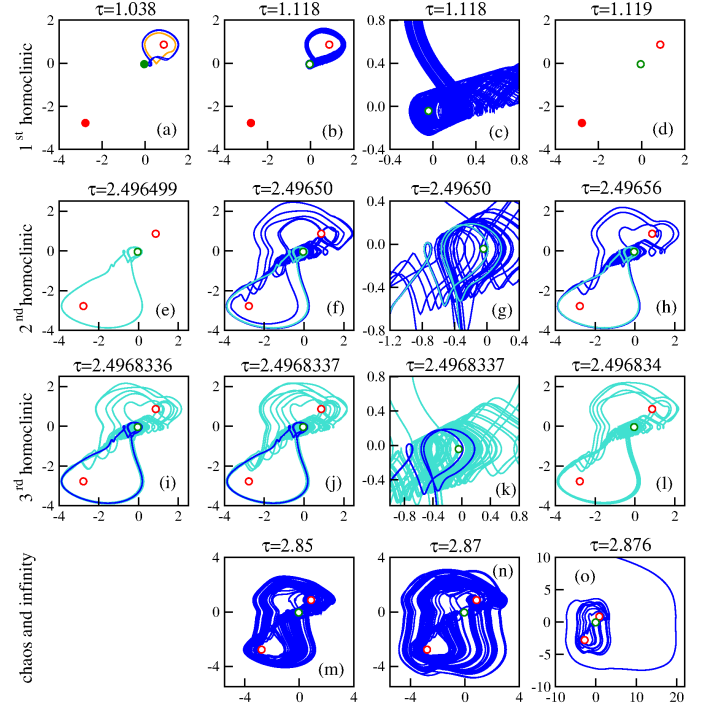


FIG. 17: Phase portraits of (S1), (10) at various τ illustrating bifurcation diagrams in Figs. 15 and 16. Notations are: fixed points $x_{1,2}^{\min}$ (red circles) and x^{\max} (green circle); filled/empty circles indicate points below/above AH bifurcations; attractors (blue, turquoise and orange lines). **1st row:** (a) Before, (b)–(c) at, and (d) after 1st homoclinic bifurcation. (a) Three coexisting attractors: stable fixed point x_1^{\min} (red filled circle) and two limit cycles around x_2^{\min} (orange and blue lines). (b)–(c) Small chaos born from the homoclinic loop of the saddle cycle around x^{\max} (blue line) (cf. with Fig. 4(c)) coexists with stable fixed point x_1^{\min} . (d) Fixed point x_1^{\min} is the only attractor. **2nd row:** (e) Before, (f)–(g) at, and (h) after the 2nd homoclinic bifurcation. (e) Small cycle around x_1^{\min} is the only attractor (turquoise line). (f)–(g) Birth of large chaos from the homoclinic loop of the saddle cycle around x^{\max} (blue line). (h) Large chaos coexists with the small limit cycle around x_1^{\min} (turquoise line). **3rd row:** (i) Before, (j)–(k) at, and (l) after 3rd homoclinic bifurcation. (i) Small cycle (turquoise line) coexists with large homoclinic chaos (blue line). (j)–(k) Small attractor (turquoise line) just before homoclinic bifurcation (blue line). (l) Large chaos is the only attractor. **4th row:** (m) Chaos embracing all fixed points at large τ , (n) chaotic attractor grows in size, and (o) trajectory goes to infinity at τ above some critical value.

ance of the local attractor through a homoclinic bifurcation, bistability may either occur, or fail to occur. However, the exact nature of homoclinic bifurcations does not seem to change the general sequence of events as τ grows, which has been confirmed also with a number of additional examples not detailed here due to the lack of space.

With this, in addition to our initial hypothesis, our analysis revealed that when τ becomes too large, even

the large attractor disappears, and the system goes to infinity. Moreover, at all positive values of delay, there is a broad range of initial conditions, from which the phase trajectory goes to infinity. Importantly, as the delay grows from zero, the basins of all attractors located at or near the minima shrink, implying that at large delay the choice of initial conditions leading to one of the finite attractors can become quite challenging. This observation suggests that in applications to optimization, it is best to start from zero delay with arbitrary initial conditions, from which there is a guaranteed convergence to one of the local minima, since there is no attractor at infinity. After that, one can gradually increase the delay and observe how the large attractor is born and then destroyed, and note the latter value. Then one can start from zero delay again and raise the delay to just beyond the death of the large attractor, after which the delay could be adiabatically decreased to zero. As a result, the system would end up at one of the minima, which could

be the lowest minimum under some conditions. Thus, we are satisfied with our ability to qualitatively predict the order of events induced by the increase of time delay in a dynamical system implementing a “gradient descent” with a double-well cost function. The acquired knowledge allows us to proceed to the study of the systems of the form (S1) with a multi-well cost function V [1].

VI. ACKNOWLEDGEMENTS

The authors are grateful to Dmitri Tseluiko for helpful discussions about Shilnikov’s theorem, and for help in preparing Figures 10(k)-(o); and to Alexander Balanov for help in creating software to solve DDEs numerically. C.J.M. was supported by EPSRC (UK) during his PhD studies in Loughborough University.

-
- [1] N. Janson and C. Marsden, Optimization by delay, submitted (2019).
 - [2] C. Floudas and C. Gounaris, *Journal of Global Optimization* **45**, 3 (2009).
 - [3] C. Floudas and P. P.M., *Encyclopedia of Optimization, 2nd Ed.* (Springer, 2008).
 - [4] G. Arfken and H. Weber, *Mathematical Methods for Physicists, 6th ed.* (Academic Press, 1985).
 - [5] M. Hirsch, S. Smale, and R. Devaney, *Differential equations, dynamical systems, and an introduction to chaos* (Academic Press Boston, 2004).
 - [6] H. Kushner and D. Clark, *Stochastic Approximation Methods for Constrained and Unconstrained Systems*, Applied Math. Science Series 26 (Springer, 1978).
 - [7] S. Kirkpatrick, C. Gelatt Jr, and M. Vecchi, *Science* **220**, 671 (1983).
 - [8] F. Aluffi-Pentini, V. Parisi, and F. Zirilli, *Journal of Optimization Theory and Applications* **47**, 1 (1985).
 - [9] S. Gelfand and S. Mitter, *SIAM J. Control Optim.* **29**, 999?1018 (1991).
 - [10] J. King, S. Yarkoni, J. Raymond, I. Ozfidan, A. King, M. Mohammadi Nevisi, J. Hilton, and C. McGeoch, *Tech. Rep., D-Wave Technical Report Series, 14-1003A-C* (2017).
 - [11] V. Arnold, *Geometrical Methods in the Theory of Ordinary Differential Equations. 2nd ed.* (Springer-Verlag, 1988).
 - [12] L. Shilnikov, A. Shilnikov, D. Turaev, and L. Chua, *Methods of qualitative theory in nonlinear dynamics, Part 2*, vol. 5 (World Scientific Pub Co Inc, 2001).
 - [13] J. Guckenheimer and P. Holmes, *Nonlinear oscillations, dynamical systems, and bifurcations of vector fields*, vol. 42 (Springer-Verlag, 1997).
 - [14] S.-N. Chow, *Journal of Differential Equations* **15**, 350 (1974).
 - [15] J. Kaplan and J. Yorke, *Journal of Differential Equations* **23**, 293 (1977).
 - [16] U. an der Heiden and H.-O. Walther, *Journal of Differential Equations* **47**, 273 (1983).
 - [17] S.-N. Chow, X.-B. Lin, and J. Mallet-Paret, *Journal of Dynamics and Differential Equations* **1**, 3 (1989).
 - [18] J. Wei, *Nonlinearity* **20**, 2483 (2007).
 - [19] C. Huang, Z. Yang, T. Yi, and X. Zou, *Journal of Differential Equations* **256**, 2101 (2014).
 - [20] J. K. Hale and X.-B. Lin, *Journal of Differential Equations* **65**, 175 (1986).
 - [21] R. Nussbaum, *Journal of Differential Equations* **14**, 360 (1973).
 - [22] R. Nussbaum, *Annali di Matematica* **101**, 263 (1974).
 - [23] J. Kaplan and J. Yorke, *Journal of Mathematical Analysis and Applications* **48**, 317 (1974).
 - [24] J. Kaplan and J. Yorke, *SIAM Journal on Mathematical Analysis* **6**, 268 (1975).
 - [25] J. Mallet-Paret, *Journal of Differential Equations* **22**, 331 (1976).
 - [26] R. Nussbaum, *Journal of Mathematical Analysis and Applications* **55**, 699 (1976).
 - [27] S.-N. Chow and B. Deng, *Transactions of the American Mathematical Society* **312**, 539 (1989).
 - [28] H.-O. Walther, *Nonlinear Analysis: Theory, Methods & Applications* **5**, 775 (1981).
 - [29] H.-O. Walther, *Transactions of the American Mathematical Society* **290**, 213 (1985).
 - [30] H.-O. Walther, *Dynamical systems and ergodic theory*, Banach Center Publications **23**, 243 (1989).
 - [31] H.-O. Walther, *Bifurcation from a saddle connection in functional differential equations: An approach with inclination lemmas* (Instytut Matematyczny Polskiej Akademii Nauk, 1990), URL <http://eudml.org/doc/268509>.
 - [32] L. Shilnikov, *Dokl. Akad. Nauk SSSR* **160**, 558 (1965).
 - [33] L. Shilnikov, *Mathematics of the USSR-Sbornik* **6**, 427 (1968).
 - [34] J. Hale and X.-B. Lin, *Nonlinear Analysis: Theory, Methods & Applications* **10**, 693 (1986).
 - [35] B. Krauskopf and H. Osinga, *Chaos: An Interdisciplinary Journal of Nonlinear Science* **9**, 768 (1999).
 - [36] B. Krauskopf and K. Green, *Journal of Computational Physics* **186**, 230 (2003).

- [37] J. Hale and S. Verduyn Lunel, *Introduction to functional differential equations*, vol. 99 (Springer, 1993).
- [38] *Journal of Differential Equations* **50**, 260 (1983).
- [39] P. Aguirre, B. Krauskopf, and H. Osinga, *SIAM Journal on Applied Dynamical Systems* **12**, 1803 (2013).
- [40] P. Aguirre, B. Krauskopf, and H. M. Osinga, *Journal of Computational Dynamics* **1**, 1 (2014).
- [41] A. Balanov, N. Janson, V. Astakhov, and P. McClintock, *Phys. Rev. E* **72**, 026214 (2005).
- [42] J. Losson, M. C. Mackey, and A. Longtin, *Chaos: An Interdisciplinary Journal of Nonlinear Science* **3**, 167 (1993).
- [43] S. R. Taylor and S. A. Campbell, *Phys. Rev. E* **75**, 046215 (2007).
- [44] In ODEs, a homoclinic solution would be called doubly asymptotic to the fixed point (here $x=0$), which means that it approaches this point when t tends not only to positive, but also to negative, infinity, given that time can be reversed. However, in DDEs time cannot be generally reversed, so the term “doubly asymptotic” might not be fully appropriate here.

Delay-induced homoclinic bifurcations in bistable dynamical systems

Supplementary Note

Natalia B. Janson^{1,*} and Christopher J. Marsden^{1,&}

¹ Department of Mathematical Sciences, Loughborough University, Loughborough LE11 3TU, UK

* N.B.Janson@lboro.ac.uk

& chris.j.marsden@gmail.com

In this Supplementary Note we show how the standard analytical tools can be applied to predict the local behavior of the delay-differential equation (DDE) of the following form

$$\dot{x} = f(x_\tau), \quad f(z) = -\frac{dV(z)}{dz}, \quad (\text{S1})$$

where $x, f, V, z \in \mathbb{R}$, $x_\tau = x(t - \tau)$, $V(z)$ is some landscape function, and $f(z)$ is a twice differentiable function. Specifically, by performing linear stability analysis, we will reveal at what values of time delay τ the fixed points at the minima of $V(z)$ change from stable nodes to stable focuses and then undergo Andronov-Hopf bifurcation. Doing so will allow us to predict at what τ around the given fixed point a stable periodic oscillation could be observed.

We also analyse the stability of the fixed points located at the maxima of $V(z)$. Although these points remain unstable for any positive τ and thus unobservable in an experiment, perhaps counterintuitively, the parameters characterising their instability affect the observable behavior of the system. For example, it is possible for the manifolds of an unstable fixed point of a saddle-focus type to close and to form a homoclinic loop. As the parameter of the system changes, this loop breaks down and can give birth to a new attractor, which will extend well beyond the close vicinity of the relevant point. According to Shilnikov's theorem, this new attractor can be either periodic or chaotic, and its nature is determined by the local properties of the respective unstable point [32], [S1, S2]

We start from performing linear stability analysis of the fixed points x^* of (S1), which satisfy

$$f(x^*) = 0. \quad (\text{S2})$$

Unlike a system of ordinary differential equations (ODEs), a DDE is an infinite-dimensional dynamical system because in order to solve such an equation, as an initial condition one needs to specify a function on an interval, namely, $x(t) = \varphi(t)$ on $t \in [-\tau, 0]$, which contains infinitely many points. With this, if we wish to represent the dynamics of a DDE in the phase space by analogy with what is done for ODEs, we need to appreciate that the full state of a DDE at time t would be a function on an interval $[t - \tau, t]$, and therefore the dimension of the respective phase space is infinity [S3]. As a single state of the DDE, the fixed point can be viewed as a constant function $x(t) = x^*$ on an interval $[t - \tau, t]$, which stays the same at all times t . By analogy with the linear stability analysis of ODEs, we need to slightly perturb the system away from the fixed point. So we introduce

$$x = x^* + X, \quad |X| \ll 1,$$

where $X(t)$ is the perturbation of the fixed point x^* . Given that $\dot{x} = \dot{X}$, substitute the latter into (S1) to obtain

$$\dot{X} = f(x^* + X_\tau),$$

where $X_\tau(t) = X(t - \tau)$. Because X is small, $|X_\tau| \ll 1$, and we can approximate the above equation by expanding f in Taylor series and keeping the linear terms only

$$\dot{X} \approx f(x^*) + JX_\tau,$$

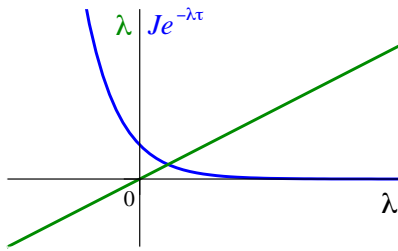


FIG. S1: Illustration of solution to Eq. (S4). Figure shows the graphs of λ (green line) and of $Je^{-\lambda\tau}$ for positive τ and J (blue line). These two curves are guaranteed to intersect at some positive and real value of λ , which means that the local maxima of the landscape $V(z)$ in (S1) are always unstable.

where $J = \frac{df}{dz}$ at $z = x^*$. With account of (S2), we obtain the so-called *linearized equation*, which holds as long as $X(t)$ stays small

$$\dot{X} = JX_\tau. \quad (\text{S3})$$

We assume that the linear DDE (S3) has exponential solutions, i.e.

$$X(t) = Ae^{\lambda t}, \quad A = \text{const},$$

which on substitution back into (S3) gives

$$\lambda = Je^{-\lambda\tau}. \quad (\text{S4})$$

Equation (S4) is called the characteristic equation, and its roots λ are called the eigenvalues of the fixed point. Eq. (S4) has a countably infinite number of generally complex roots. The eigenvalue with the largest real part is called the leading eigenvalue. If the solution of the characteristic equation has only negative real parts, then the respective fixed point is stable. If there are eigenvalues with positive real parts, then the fixed point is unstable. If the real part of the leading eigenvalue is zero, the stability cannot be deduced to linear order. Although an infinite number of eigenvalues could potentially present a challenge in the stability analysis, it has been proved that there are only a finite number of eigenvalues to the right of any vertical line in the complex plane [S4]. This means, that the number of eigenvalues with a positive real part can only be finite, so to determine the stability of a fixed point, we need to consider only a finite number of values.

Note, that the fixed points corresponding to the maxima of $V(z)$ are unstable at any $\tau \geq 0$. Indeed, at a maximum of $V(z)$, $J = \frac{df}{dz} = -\frac{d^2V}{dz^2} > 0$. With a positive J , Eq. (S4) always has a real positive root λ (see Fig. S1 illustrating the solution).

The solutions λ of (S4) can be expressed in terms of the Lambert function $W(z)$, also called the product log function. Lambert function is a complex-valued function of a complex argument defined as an inverse of the function $h(z) = ze^z$, where $z, h \in \mathbb{C}$ [S5, S6]. The function $W(z)$ is formed of solutions w of the equation

$$we^w = z, \quad (\text{S5})$$

so that for every value of z there is a countable infinity of the values of w . In applications to the stability of DDEs, only real arguments z of $W(z)$ are used, which means that only the values of $W(z)$ corresponding to the cross-section along $Im[z]=0$ are relevant to the problem. From now on, we will assume that z are real. The function $W(z)$ with $z \in \mathbb{R}$ has countably many branches W_k , $k = 0, \pm 1, \pm 2, \dots$, and W_0 is called the principal branch. In Fig. S2, real (upper panel) and imaginary (lower panel) parts of $W(z)$ are shown as a function of z .

The solutions λ of (S4) are equal to

$$\lambda_k = \frac{W_k(J\tau)}{\tau} = \frac{JW_k(z)}{z}, \quad (\text{S6})$$

where W_k is the k -th branch of $W(z)$. Note, that in (S6), for $z > -\frac{1}{e}$ the principal branch $W_0(z)$ takes real values only. In Fig. 7 eigenvalues λ_k are illustrated as functions of $(J\tau)$ for the fixed points at local maxima of the landscape V of (S1) with $J > 0$. As confirmed by Fig. 7, such fixed points are always unstable because one of their eigenvalues is

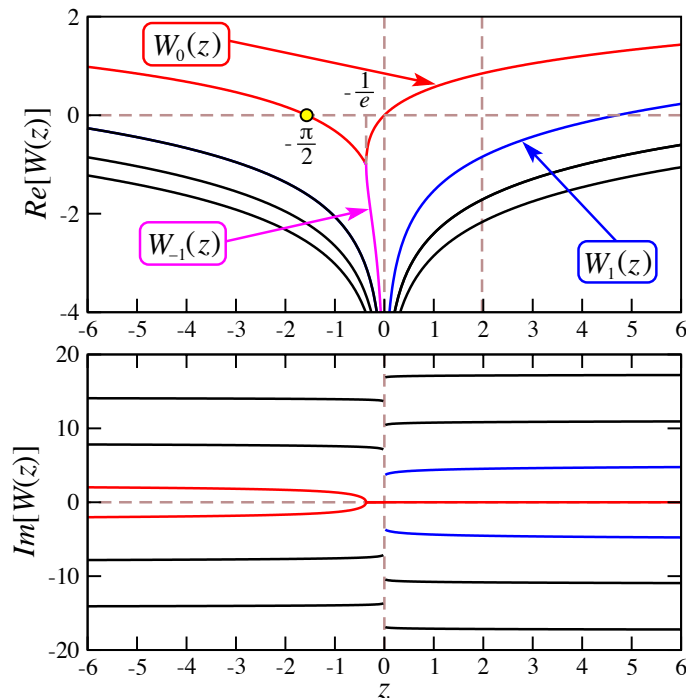


FIG. S2: Real (upper panel) and imaginary (lower panel) parts of Lambert Function $W(z)$, assuming that z takes only real values. Red line shows the principal branch $W_0(z)$, magenta line shows $W_{-1}(z)$, and blue line shows $W_1(z)$.

real and positive at all positive values of τ . Note, that at $\tau=0$ these fixed points have only one positive real eigenvalue equal to J . Indeed, at $\tau=0$ (3) becomes a first order ODE, in which fixed points have only one real eigenvalue equal to the derivative J of the right-hand side. Fig. 6 shows eigenvalues as functions of $(|J|\tau)$ for the fixed points at local minima of V with $J<0$. One can see that for small τ these fixed points are stable, but as τ increases, they become unstable.

Next, we calculate the values of τ , at which Andronov-Hopf (AH) bifurcation occurs for the given fixed point. If a stable fixed point undergoes AH bifurcation, the point becomes unstable and possibly a stable periodic solution is born from it, thus giving rise to oscillatory behavior of the system. The first condition of AH bifurcation is that the real part of $W_0(J\tau)$ must be equal to zero. Given J , we need to determine the respective value of τ at which (S4) has purely imaginary roots, i.e. $\lambda=\pm\beta i$ with $\beta\in\mathbb{R}$. Substituting this into (S4) gives

$$\beta i - J e^{-\beta i \tau} = 0.$$

This can be written as

$$\beta i - J[(\cos(\beta\tau) - i \sin(\beta\tau))] = 0.$$

Separating real and imaginary parts gives

$$\cos(\beta\tau) = 0, \tag{S7}$$

$$\beta + J \sin(\beta\tau) = 0. \tag{S8}$$

Equation (S7) has infinitely many solutions in the form of conjugate pairs,

$$\beta = \frac{(\frac{\pi}{2} \pm n\pi)}{\tau}, \quad n = 0, 1, 2, \dots, \tag{S9}$$

which we then substitute into (S8) to obtain

$$\tau = -\frac{(\frac{\pi}{2} + n\pi)}{J(-1)^n}, \quad n = 0, 1, 2, \dots, \tag{S10}$$

which will have the same τ for both components of the conjugate pair. Assume that we consider the local minima of the landscape $V(z)$, at which $J < 0$. Also, in this work we assume that τ can only be positive, and to ensure that this is the case in (S10) n must be *even*. The first Andronov-Hopf bifurcation occurs for the smallest even value of n , therefore we take $n=0$ to obtain

$$\tau_{AH} = -\frac{\pi}{2J} = \frac{\pi}{2|J|}. \quad (\text{S11})$$

This result is consistent with the earlier predictions, obtained with a very different approach, of the existence of periodic solutions in DDEs (4) for a special form of $g(z)$ as discussed in Sec. IIA. At larger even values of n in (S10), more complex conjugate pairs of eigenvalues cross the imaginary axis from below.

The second criterion to be satisfied for an Andronov-Hopf bifurcation to occur is [S4, S7]

$$\left. \frac{dRe(\lambda)}{d\tau} \right|_{\tau=\tau_{AH}} > 0. \quad (\text{S12})$$

To verify this, differentiate both parts of (S4) with respect to τ to obtain

$$\frac{d\lambda}{d\tau} = -Je^{-\lambda\tau} \left(\lambda + \tau \frac{d\lambda}{d\tau} \right). \quad (\text{S13})$$

Assume that $\lambda = \alpha + i\omega$ with $\alpha, \omega \in \mathbb{R}$, and substitute into (S13). Separating real and imaginary parts gives

$$\begin{aligned} \frac{d\alpha}{d\tau} &= -Je^{-\alpha\tau} \cos(\omega\tau) \left(\alpha + \tau \frac{d\alpha}{d\tau} \right) - Je^{-\alpha\tau} \sin(\omega\tau) \left(\omega + \tau \frac{d\omega}{d\tau} \right), \\ \frac{d\omega}{d\tau} &= -Je^{-\alpha\tau} \cos(\omega\tau) \left(\omega + \tau \frac{d\omega}{d\tau} \right) + Je^{-\alpha\tau} \sin(\omega\tau) \left(\alpha + \tau \frac{d\alpha}{d\tau} \right). \end{aligned} \quad (\text{S14})$$

Eq. (S12) implies

$$\left. \frac{d\alpha}{d\tau} \right|_{\tau=\tau_{AH}} > 0. \quad (\text{S15})$$

At AH bifurcation $\alpha=0$ and $\omega=\beta$. By setting in (S9) $n=0$ and substituting τ from (S11) we obtain

$$\begin{aligned} \alpha &= 0, \\ \omega &= \frac{\pi}{2\tau_{AH}} = -J. \end{aligned} \quad (\text{S16})$$

Substituting these values into (S14) gives

$$\begin{aligned} \frac{d\alpha}{d\tau} &= J^2 + \frac{\pi}{2} \frac{d\omega}{d\tau}, \\ \frac{d\omega}{d\tau} &= -\frac{\pi}{2} \frac{d\alpha}{d\tau}. \end{aligned} \quad (\text{S17})$$

Combining these equations to exclude $\frac{d\omega}{d\tau}$ gives

$$\frac{d\alpha}{d\tau} = \frac{4J^2}{(4 + \pi^2)} > 0. \quad (\text{S18})$$

So we have verified both criteria for the occurrence of AH bifurcation, in which the fixed point loses stability. In the numerical simulations performed here, the bifurcation is always supercritical and leads to the birth of a stable limit cycle.

Equation (S10) can also be used to find the values of τ at which the fixed points at the maxima of the landscape $V(z)$ undergo AH bifurcation. In this case $J \geq 0$, therefore, to ensure the positivity of τ , n must be *odd*. Again choosing the smallest value of n , $n=1$, gives

$$\tau_{AH}^s = \frac{3\pi}{2J}. \quad (\text{S19})$$

Such fixed points would remain unstable for any τ . However, as a result of this bifurcation, a saddle periodic orbit could be born from the fixed point, together with its stable and unstable manifolds, which will affect the dynamics of the system. Further complex conjugate pairs will cross the imaginary axis for odd values of n in (S10).

This theory can be extended to equations of the form (2) with an n -dimensional vector x . The approach will be similar, however, an $n \times n$ Jacobian matrix will be involved, resulting in an order- n quasi-polynomial for the characteristic equation, which can be analysed to deduce the relevant bifurcations.

-
- [S1] L. Shilnikov and A. Shilnikov, *Shilnikov or Šilnikov bifurcation* (2007 (accessed 22 July 2018)), URL http://www2.gsu.edu/~matals/lp/lp_papers/saddle-focus_s.pdf.
- [S2] V. Afraimovich, S. Gonchenko, L. Lerman, A. Shilnikov, and D. Turaev, *Regular and Chaotic Dynamics* **19**, 435 (2014).
- [S3] M. Roussel, *Delay-differential equations* (2005 (accessed 22 July 2018)), URL <http://people.uleth.ca/~roussel/nld/delay.pdf>.
- [S4] J. Hale and S. Verduyn Lunel, *Introduction to Functional Differential Equations* (Springer-Verlag New York, 1993).
- [S5] R. Corless, G. Gonnet, D. Hare, D. Jeffrey, and D. Knuth, **5**, 329 (1996).
- [S6] A. Dubinov and I. Dubinova, *Journal of Plasma Physics* **71**, 715 (2005).
- [S7] J. Hale, *Functional differential equations* (Springer-Verlag New York, 1971).